energies

IMPACT FACTOR 3.2

CITESCORE 7.3

Article

Hotspots of Current Energy Potential in the Southwestern Tropical Atlantic

Tarsila Sousa Lima, Syumara Queiroz, Maria Eduarda Américo Ishimaru, Eduardo José Araújo Correia Lima, Márcio das Chagas Moura and Moacyr Araujo

MDPI

https://doi.org/10.3390/en19020329

energies

MDPI

Article

Hotspots of Current Energy Potential in the Southwestern Tropical Atlantic

Tarsila Sousa Lima [1,2,3,*], Syumara Queiroz [1,2,3], Maria Eduarda Américo Ishimaru [1,2], Eduardo José Araújo Correia Lima [1,2], Márcio das Chagas Moura [2] and Moacyr Araujo [1,2,3]

[1] Laboratory of Estuarine and Coastal Physical Oceanography (LOFEC), Department of Oceanography, Federal University of Pernambuco, Av. Arquitetura, Recife 50740-550, Pernambuco, Brazil
[2] Center for Risk Analysis, Reliability Engineering and Environmental Modeling (CEERMA), Federal University of Pernambuco, Recife 50740-550, Pernambuco, Brazil
[3] Brazilian Research Network on Global Climate Change–Rede Clima, Av. dos Astronautas, 1758-Jardim da Granja, São José dos Campos 12227-010, São Paulo, Brazil
* Correspondence: tarsila.lima@ufpe.br

Abstract

In the effort to mitigate climate change, the Marine Hydrokinetic (MHK) energy from ocean currents emerges as an important renewable source due to its large potential, although it remains underexploited. In the Southwestern Tropical Atlantic, surface potentials linked to the North Brazil Current (NBC) are known, but the subsurface North Brazil Undercurrent (NBUC) remained unquantified. This study addressed this gap by applying a two-step approach using more than 20 years of high-resolution (1/12°) climatological and daily reanalysis data to estimate current power density (CPD) throughout the water column along the Brazilian shelf (4° N–12° S), with focus on energetic hotspots where maximum CPD exceeds 1000 W m^{-2}. The climatological analysis revealed 12 persistent hotspots (H1–H12). Daily analyses show highly energetic but seasonally variable surface hotspots north of 4° S linked to the NBC (H4–H12; >885 W·m^{-2}) and weaker but more stable subsurface hotspots south of 4° S associated with the NBUC at depths of 130–266 m (H1–H3; 831–808 W·m^{-2}). These patterns are likely influenced by flow–topography interactions along the continental margin. Overall, subsurface resources exhibit greater reliability than surface counterparts, highlighting the importance of incorporating subsurface dynamics in future MHK assessments and development along the Brazilian margin.

Keywords: marine hydrokinetic energy; current power density; western boundary current; Southwestern Tropical Atlantic; North Brazil Undercurrent

Received: 28 November 2025
Revised: 27 December 2025
Accepted: 28 December 2025
Published: 9 January 2026

1. Introduction

Climate change is intensifying pressures on global energy systems, demanding an accelerated transition towards decarbonization and energy security. Replacing fossil fuels with renewable sources is considered essential to meet climate goals, ensure energy resilience, and address growing socioeconomic demands [1,2]. While renewable energy sources have expanded to reach nearly 30% of the global electricity mix, mature technologies like hydropower, biomass, geothermal, wind, and solar dominate this growth [3]. Conversely, marine energy technologies are under development stage, contributing approximately 1 TWh to the global electricity generation in 2024, with the largest contributions coming from countries in Asia and Europe, and associated mainly with wave and tidal energy [3,4]. In this scenario, energy

generation from ocean currents remains relatively underexplored compared to other renewable sources, despite its strong potential, the abundance of the reserve of ocean current energy and its capacity to diversify the electricity mix [5].

From a broader security perspective, marine renewable energy is increasingly framed within sustainable development goals that integrate environmental, economic, and social dimensions of human well-being. In this context, security is commonly treated as a system of interdependent pillars—environmental, economic, and social—such that sustainable development actions are directly connected to a "secure future" and societal well-being [6]. This framing is particularly relevant for marine energy because responsible deployment requires balancing energy supply benefits with environmental risks and societal acceptance, and because resource reliability can influence economic feasibility and energy-system resilience. Accordingly, marine renewable energy planning is often described as needing to account for socioeconomic needs, environmental concerns/risks, and social perception to support responsible implementation [7,8], while comparative assessments describe ocean energy as a low-carbon option with low-to-moderate impacts on ecosystems and on health and safety relative to other sources [1]. In Brazil—where ocean renewable resources remain largely underexploited—more temporally stable marine resources are also highlighted as potentially valuable for supporting reliable supply in contexts where alternatives may be scarce or expensive, reinforcing the practical motivation for quantifying not only mean power but also the stability of current-driven resources [9].

In the global transition towards a sustainable energy matrix, ocean currents represent a unique renewable resource, offering a predictable consistent speed and direction for baseload power generation. The high power density of marine hydrokinetic (MHK) energy is a direct result of the density of seawater, which is approximately 800 times denser than air; consequently, the kinetic power of a 1 $m \cdot s^{-1}$ water flow is equivalent to that of a 9.3 $m \cdot s^{-1}$ wind [10,11]. This immense potential has spurred research into technologies capable of harnessing this energy, especially within the most energetic regions of the world's oceans. The technological landscape for MHK is diverse, encompassing a range of Marine Current Energy Devices (MCEDs). The most common devices are rotating systems, including horizontal-axis turbines, which resemble underwater wind turbines, and cross-flow turbines, whose rotational axis can be horizontal or vertical [12,13]. However, as the most powerful currents are often located in deep water far from shore, the industry is increasingly focused on advanced floating and tethered systems. Successful prototypes, such as the 100 kW 'Kairyu' floating horizontal-axis turbine system tested in Japan's Kuroshio Current [14], and innovative concepts like underwater kites [10], demonstrate the technological push to access these challenging deep-water resources where traditional fixed-bottom installations are unfeasible.

Despite these technological advancements, the commercial exploitation of ocean currents remains in its early stages. A primary barrier is that the price of generated electricity is not yet competitive with present wholesale prices [15]. This is due to the immense technical hurdles and high capital and operational expenditures. Since strong currents are often located far from shore, expenses are significantly increased by the logistical complexity and specialized vessels required to build, install, and maintain robust systems in energetic and corrosive sub-sea environments [16]. Key engineering challenges include designing foundations for complex seabed and developing reliable mooring systems for deep waters [4,9]. Consequently, research and development efforts are concentrated on the most promising locations where the sheer scale of the resource can overcome these economic barriers, such as, for example, in the Kuroshio Current (e.g., [14,17]), Gulf Stream (e.g., [18]) and Agulhas Current (e.g., [19]), important Western Boundary Currents (WBCs). These are fast, narrow, and deep-reaching currents that play a crucial role in the planet's climate by transporting

vast amounts of heat poleward [20]. Their jet-like structure and inherent variability, caused by meanders and the shedding of eddies, present both a massive energy resource and a complex engineering challenge, making detailed resource characterization a critical first step for any potential project [21,22].

The Southwestern Tropical Atlantic (SWTA), offshore of Northeast and North Brazil (Figure 1), is dominated by a powerful and complex WBC system formed when the southern South Equatorial Current (sSEC) bifurcates on the Brazilian margin—between 13° and 17° S in the upper 200 m. This originates the northward-flowing North Brazil Undercurrent (NBUC) and the southward Brazil Current (BC) [20,23–25]. The NBUC follows under the surface along the continental slope, shallowing towards the equator, until encountering the central South Equatorial Current (cSEC) originating the North Brazil Current (NBC) [26]. Therefore, the BC and NBUC/NBC system constitute the dominant energetic feature of the western boundary circulation in this region.

The NBUC has a nearshore core position approximately 50 km from the Brazilian coast, reaching down to about 900 m in depth, with velocities ranging from about 0.5 $m \cdot s^{-1}$ near the surface to nearly 1.0 $m \cdot s^{-1}$ between 180 and 250 m [23,26–30]. The current has a marked seasonality induced by the latitudinal change in the sSEC bifurcation, with stronger/weaker currents when the bifurcation is in its southernmost/northernmost position around July/November [24,26,31]. The NBC flows in the between 0–100 m to the northwest along the shelf break with velocities of ~1.0 $m \cdot s^{-1}$ [32,33], reaching a maximum transport in July–August and a minimum in April–May, influenced by the Intertropical Convergence Zone (ITCZ) [34]. In contrast, the BC is weaker with typical surface core velocities of about 0.4–0.7 $m \cdot s^{-1}$ with the seasonality opposite to the NBUC, also induced by the sSEC bifurcation [35,36].

The currents in the SWTA interact with the Northeast continental margin, modulating the boundary flow, and mesoscale activity (e.g., [26,37]). The shelf width varies between 100 and 200 with a shelf break depth ~60–80 m, and a rapid transition to abyssal depths exceeding 3000 m, eventually interrupted by plateaus (Touros High offshore Rio Grande do Norte and Pernambuco Plateau), seamounts and oceanic islands from the Fernando de Noronha chain [38–41]. The vertical thermohaline structure is characterized by well-defined density stratification rather than by sharp water-mass boundaries. The upper ~100–150 m are dominated by light waters with σ_θ < 25.7 $kg \cdot m^{-3}$, overlying a denser thermocline layer with $\sigma_\theta \approx$ 25.7–26.8 $kg \cdot m^{-3}$ extending down to about 600 m. Below this, intermediate levels are occupied by waters with $\sigma_\theta \approx$ 26.8–27.3 $kg \cdot m^{-3}$ (~600–1200 m), and deeper layers are composed of even denser waters with σ_θ > 27.3–27.7 $kg \cdot m^{-3}$, reaching $\sigma_\theta \gtrsim$ 27.9–28.0 $kg \cdot m^{-3}$ near the bottom [42,43]. This monotonic increase in density with depth reflects the typical South Atlantic layering, often associated with Tropical Water, South Atlantic Central Water, Antarctic Intermediate Water, North Atlantic Deep Water, and Antarctic Bottom Water [43,44] and directly influences the spatial patterns of seawater density used in the current power density calculations.

Altogether, the combination of strong western boundary currents and salinity-induced denser water masses suggests the SWTA as a dynamically active region and a natural hotspot of ocean current energy. However, its full hydrokinetic potential remains one of the least explored among Brazil's renewable resources. A foundational review by Shadman et al. [9] identified a significant surface potential (500 $W \cdot m^{-2}$ associated with ~1.52 $m \cdot s^{-1}$ current speed) along the Brazilian Equatorial Margin, but this assessment was limited to the upper 50 m of the water column. As a result, the energetic contribution of the powerful, undersurface NBUC has been largely unassessed, representing a critical knowledge gap in the evaluation of the region's marine energy portfolio. The central hypothesis here is that the subsurface components of the Western Boundary Current

system in the SWTA, primarily the NBUC, represent a substantial source of renewable energy. Therefore, this study addresses the subsurface gap by delivering the first high-resolution, multi-decadal assessment of both surface and subsurface marine current energy resources in the SWTA. Beyond the regional contribution, this work introduces a two-stage, spatially targeted methodology to identify and evaluate persistent hotspots across depth layers, enabling cross-site comparisons and parametric resource characterization. These results expand the geographic and dynamical scope of marine energy research, offering new insights into the role of tropical boundary current systems in renewable energy planning and infrastructure design—a topic of growing relevance for the global blue economy and climate-resilient energy transitions.

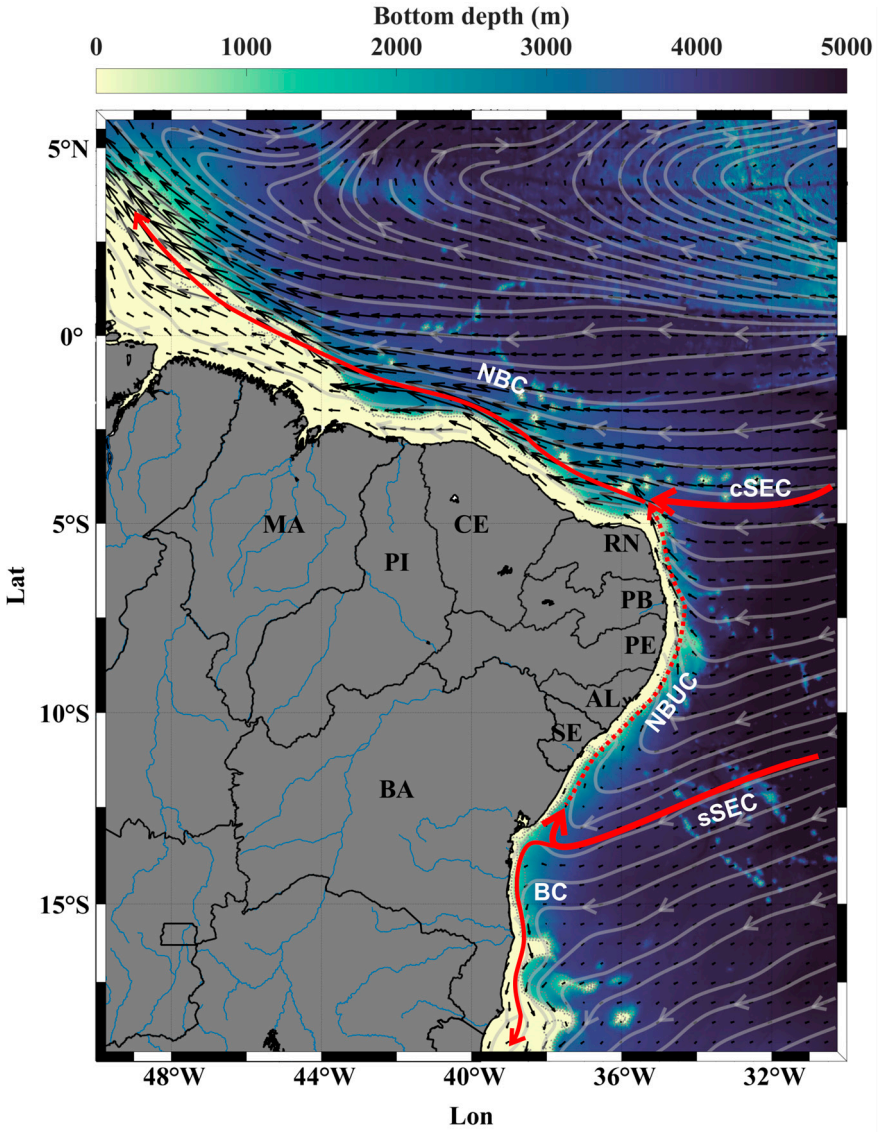

Figure 1. Study region showing bottom depth (colormap), current vectors (black arrows) and streamlines (grey arrows) in the Southwestern Tropical Atlantic (SWTA). Schematic red arrows demonstrate the direction of the zonal flows for the central and southern branches of the South Equatorial Current (cSEC and sSEC, respectively) and the Western Boundary Currents: North Brazil Current (NBC), North Brazil Undercurrent (NBUC, dashed) and Brazil Current (BC). Northeast Brazil states: Maranhão (MA), Piauí (PI), Ceará (CE), Rio Grande do Norte (RN), Paraíba (PB), Pernambuco (PE), Alagoas (AL), Sergipe (SE), and Bahia (BA). Gray streamlines depict mean surface flow pathways derived from the climatological velocity field, indicating the direction of the large-scale circulation.

2. Materials and Methods

A two-stage workflow was designed to confine daily analyses to objectively detected high-resource areas: (1) hotspot identification from climatology; then (2) extraction and analysis of daily data restricted to those hotspots. This two-stage design was chosen to (i) identify hotspots using a long-term, stable baseline rather than transient daily extremes, and (ii) make the daily analysis computationally tractable by restricting extraction to a small subset of the domain that is most relevant for marine hydrokinetic assessment. Separating hotspot delineation (from climatology) from daily characterization (within those hotspots) also improves reproducibility and reduces sensitivity to day-to-day spatial displacement of energetic cores in coarse-resolution reanalysis.

2.1. Hotspot Identification from Climatology

The climatological fields for the study region (Figure 1), were taken from the subset cmems_mod_glo_phy_my_0.083deg-climatology_P1M-m from the Copernicus Marine Global Ocean Physics Reanalysis (GLORYS12V1; DOI: https://doi.org/10.48670/moi-00021 [45]). This product provides a global eddy-resolving reanalysis with a horizontal resolution of 1/12° and 50 vertical levels, assimilating altimetry, in situ T/S profiles, and satellite SST to correct biases in temperature and salinity fields through a 3D-VAR scheme. Compared to alternatives like HYCOM [46] and ECCO [47] the GLORYS12V1 reanalysis offers full-depth coverage, higher vertical resolution, and an observation-driven assimilation scheme that better captures mesoscale dynamics. It also offers better temporal continuity than short-term in situ campaigns or regional model hindcasts, making it well suited for long-term climatological and statistical analyses. Nevertheless, it has limitations in representing small-scale processes, topographic intensification, and nearshore dynamics [26], and like most ocean reanalysis, lacks tidal forcing and wave-current interactions, which may lead to underestimated variability near the coast and in shallow regions. Despite these caveats, GLORYS12V1 has been extensively validated and provides consistent, bias-corrected ocean condition outputs that support robust long-term assessments [45].

For the climatology, monthly means spanning 23 years (1993–2016) of current velocity, salinity, and temperature were used, restricted to the upper 35 levels (surface to 902 m), as deeper currents in the study region are typically <0.5 $m \cdot s^{-1}$ and contribute negligibly to kinetic energy. Then, Current Power Density (CPD) was defined as MHK power per unit area, $W \cdot m^{-2}$ [22] as in Equation (1) with u, v as the zonal and meridional current components, respectively, in $m \cdot s^{-1}$ and ρ is the seawater density evaluated cell-wise using GSW-Python package v. 3.6.20 (https://teos-10.github.io/GSW-Python, accessed on 6 October 2025).

$$\mathrm{CPD}(t,z,y,x) = \frac{1}{2}\rho(t,z,y,x) \mid \mathbf{U}(t,z,y,x) \mid^3, \mid \mathbf{U} \mid = \sqrt{u^2+v^2} \quad (1)$$

The CPD was computed at each grid point for all evaluated depths using the annual-mean climatological fields, then derived the Maximum CPD across depth (MCPD) and its depth of occurrence. Hotspots were defined as closed MCPD = 1000 $W \cdot m^{-2}$ contour, a conservative value within the range commonly used in marine current resource assessments (e.g., 0.25- and 1.0 $kW \cdot m^{-2}$ in [48]), to delineate high-energy areas. For each closed polygon without interpolation, the minimum/maximum longitude and latitude (forming a bounding box) and the minimum/maximum MCPD depth (vertical range) were obtained. Because CPD scales with U^3, climatological monthly means yield conservative magnitudes; the climatology was used here to locate hotspots rather than to quantify high-frequency variability. Furthermore, to evaluate robustness of the hotspot definition, a sensitivity analysis was performed using thresholds of 500, 800, 1000, 1200, and 1500 $W \cdot m^{-2}$. Additionally,

the Jaccard similarity index [49] comparing the spatial overlap between the hotspots found at this threshold and the reference ones at 1000 $W \cdot m^{-2}$ is presented. A value of 1 means perfect overlap; lower values mean less similarity.

2.2. Daily Extraction and CPD Computation Restricted to Hotspots

Daily fields came from two subsets from the same Copernicus product as the climatology. The subset comprised the multi-year archive (cmems_mod_glo_phy_my_0.083deg_P1D-m, 1 January 1993 to 30 June 2021) and the interim archive (cmems_mod_glo_phy_myint_0.083deg_P1D-m, 1 July 2021 to 26 August 2025). Daily analyses were conducted only within each hotspot's longitude–latitude bounding box and MCPD-based depth range to provide a conservative and robust sampling window. Bounding boxes include surrounding lower-energy regions and therefore tend to dilute the mean CPD relative to a polygon constrained to the energetic core. This is a conservative choice for daily resource estimates because it reduces sensitivity to small-scale, locally amplified model features and to minor spatial misplacements of the energetic core from day to day as the one reported by Dossa et al. [26] for the Global Ocean Physics Reanalysis product. This choice prioritizes robustness and reproducibility in the daily hotspot time series extraction. For each day and grid cell in these windows the zonal and meridional current components, salinity and temperature were extracted from the multi-year and interim archives. Where both products provided the same date, interim values were retained; no temporal gap-filling was applied.

CPD was then recomputed at native resolution as Equation (1). For each hotspot and day, a scalar CPD value was obtained by arithmetic averaging over all valid longitude, latitude, and depth grid cells within the hotspot window. Multi-year and interim segments were concatenated, time-sorted, and deduplicated to yield continuous daily CPD series per hotspot from 1993 to 2025.

2.3. Statistical Analysis

For each hotspot, daily time series minimum, maximum, mean, median, and standard deviation were reported. Distributional properties were summarized with Tukey box-plot statistics: first quartile (Q1), third quartile (Q3), interquartile range (IQR = Q3 − Q1), whiskers defined as the most extreme non-outlier values within $[Q1 - 1.5\,\mathrm{IQR},\ Q3 + 1.5\,\mathrm{IQR}]$, and outliers beyond those bounds. Seasonal structure was characterized by the distribution of daily CPD by calendar month.

Significant differences between hotspots were tested using a one-way Analysis of Variance (ANOVA). When the null hypothesis was rejected ($p < 0.05$), Tukey's Honestly Significant Difference (HSD) post hoc test was applied to identify statistically distinct hotspots.

To characterize the statistical distribution of CPD values at each hotspot, a two-parameter Weibull probability density function (PDF) was fitted to the full time series of each location. The Weibull distribution is commonly used to describe skewed and non-negative datasets such as wind speed, wave height, and ocean current power in renewable-energy resource assessment, due to its flexibility in modeling both exponential-like and near-normal behaviors [50,51]. Furthermore, ocean surface current speed distributions have also been shown to be well approximated by Weibull forms in observational datasets, supporting its use as a compact representation of flow variability with inter-site comparisons potential [52].

The probability density function of the two-parameter Weibull distribution is defined as:

$$f(x;k,\lambda) = \frac{k}{\lambda}\left(\frac{x}{\lambda}\right)^{k-1} e^{-\left(\frac{x}{\lambda}\right)^{k}}, \quad x > 0,\ k > 0, \lambda > 0 \tag{2}$$

where x denotes the CPD value ($W \cdot m^{-2}$), k is the shape parameter and λ is the scale parameter. The shape parameter k controls the form of the distribution: values $k > 2$ indicate a unimodal distribution with moderate variance; $k < 1$ represents highly skewed data with heavy tails; and $k \approx 1$ corresponds to an exponential decay. The scale parameter λ is proportional to the characteristic magnitude of the variable (in this case, CPD) [50].

For each hotspot, CPD time series were first filtered to remove non-positive values. The Weibull parameters (k, λ) were estimated using the maximum likelihood estimation (MLE) available in the weibull_min function from the SciPy library [53], constraining the location parameter to zero (i.e., assuming that the distribution starts at zero). The resulting parameters summarize the statistical behavior of CPD at each location. Higher λ values indicate stronger typical energy availability, while variations in k reflect the shape and dispersion of energy distributions [54]. This approach allows for direct comparison of energy resource characteristics across different hotspots, avoiding site-specific distribution choices that could reduce cross-site comparability.

3. Results

The maximum hydrokinetic energy resource, quantified as MCPD, was primarily concentrated at latitudes north of 12° S, with lower values observed southward across all depths (Figure 2). The vertical distribution of this energy was closely tied to the regional western boundary current system: In the upper 50 m, the highest CPD values were found in the northern portion of the study area—where the resource is dominated by the NBC—while the energy potential in the subsurface was linked to the NBUC. In contrast, the region influenced by the BC exhibited negligible potential (<300 $W \cdot m^{-2}$). Furthermore, no MCPD was identified below a depth of 300 m, where the current velocities generally decrease to less than 0.6 $m \cdot s^{-1}$, resulting in low CPD across the entire study domain.

MCPD analysis delineated 12 persistent high-energy hotspots where potential exceeds 1000 $W \cdot m^{-2}$ (Figure 2a; Table 1 presents location and depth range). The 12 hotspots formed two geographically and dynamically distinct clusters: the eastern hotspots, along the continental slope off the coasts of Paraíba (PB), and Rio Grande do Norte (RN) (H1–H3), and the northern hotspots (H4–H12), distributed along the Brazilian Equatorial Margin offshore from Ceará (CE), Maranhão (MA), and Pará (located west of MA state). Climatologically, the Northern Group also exhibited a more intense energy potential, with MCPD values frequently exceeding 1500 $W \cdot m^{-2}$ (Figure 2a). Nevertheless, they also presented the largest seasonal variability, different from the Eastern Group, as demonstrated by the standard deviation of MCPD in Figure 2b. Additionally, the eastern hotspots were found in the subsurface (130–266 m), whereas the northern hotspots were surface features (Figure 2c). The results also show that robust core hotspots remain detectable under stricter thresholds (e.g., hotspots 1–6 at 1200 $W \cdot m^{-2}$ and hotspots 3 and 4 at >1500 $W \cdot m^{-2}$), while the most western hotspots footprint decreases with increasing threshold (Figure 2d).

The physical basis for the MCPD patterns is detailed in Figure 3. High MCPD values are a direct result of power density being concentrated in high-velocity filaments corresponding to the current's core path, where speeds often exceed 1.3 $m \cdot s^{-1}$ (Figure 3a). The variability of the resource is also primarily driven by velocity fluctuations, with speed standard deviations reaching up to 0.4 $m \cdot s^{-1}$ along the main axis of the current (Figure 3b). In contrast, while spatial variations in seawater density are present (Figure 3c), their variability is considerably smaller, with density standard deviations being an order of magnitude lower (Figure 3d), evidencing that the current variability is the main forcing for northern MCPD variability. However, denser and stabler subsurface currents lead to stable resources in the Eastern portion of the study region.

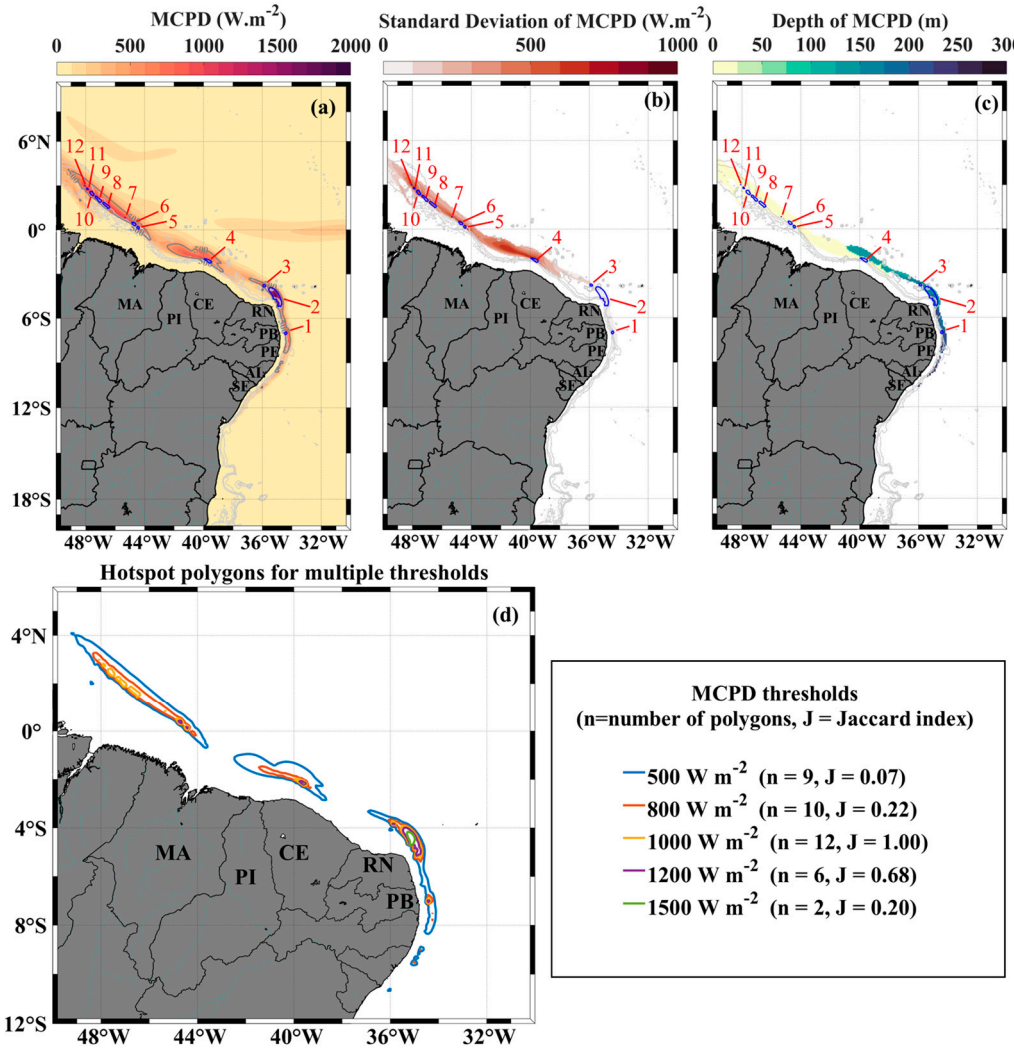

Figure 2. (**a**) Annual average and (**b**) standard deviation of the maximum current power density (MCPD) and (**c**) depth of the MCPD. Blue contours indicated by red lines and descriptors (1–12) represent hotspots of MCPD > 1000 W·m^{-2}. (**d**) Overlay of closed hotspot polygons extracted from MCPD climatology using multiple threshold values (500, 800, 1000, 1200, and 1500 W·m^{-2}). Colored contours indicate the spatial extent of hotspots identified at each threshold. The number of closed polygons (n) and the spatial similarity relative to the 1000 W·m^{-2} reference threshold, quantified using the Jaccard index (J), are reported in the legend. Higher thresholds yield fewer, more spatially confined hotspots, while lower thresholds capture broader, less persistent energetic regions.

Table 1. Coordinates and depth range (in meters) for the hotspots of current energy resource using the 1000 W·m^{-2} threshold. Depth "0" means sea surface.

Hotspot	Min. Lon	Max. Lon	Min. Lat	Max. Lat	Min. Depth	Max. Depth	Mean Depth
1	34.50311794° W	34.33045040° W	7.105770018° S	6.882931110° S	131	266	198
2	35.56277799° W	34.69037451° W	5.215420883° S	3.915738822° S	131	222	167
3	35.95514930° W	35.77659456° W	3.874762168° S	3.714923816° S	156	186	163
4	39.97185287° W	39.46325126° W	2.251789859° S	1.958868063° S	0	0	0
5	44.52622439° W	44.36119833° W	0.054347462° N	0.244547919° N	0	0	0

Table 1. *Cont.*

Hotspot	Min. Lon	Max. Lon	Min. Lat	Max. Lat	Min. Depth	Max. Depth	Mean Depth
6	44.87359625° W	44.58225517° W	0.296538033° N	0.528225899° N	0	0	0
7	45.35399403° W	45.31772390° W	0.825741777° N	0.841547764° N	0	0	0
8	46.83971696° W	46.38451470° W	1.452077887° N	1.876376457° N	0	0	0
9	47.37466777° W	46.93515169° W	1.876413530° N	2.295590423° N	0	0	0
10	47.71816236° W	47.43446094° W	2.322092614° N	2.619202279° N	0	0	0
11	47.93009985° W	47.82045592° W	2.732593635° N	2.845629499° N	0	0	0
12	48.09052323° W	48.06963931° W	2.987223703° N	3.015971091° N	0	0	0

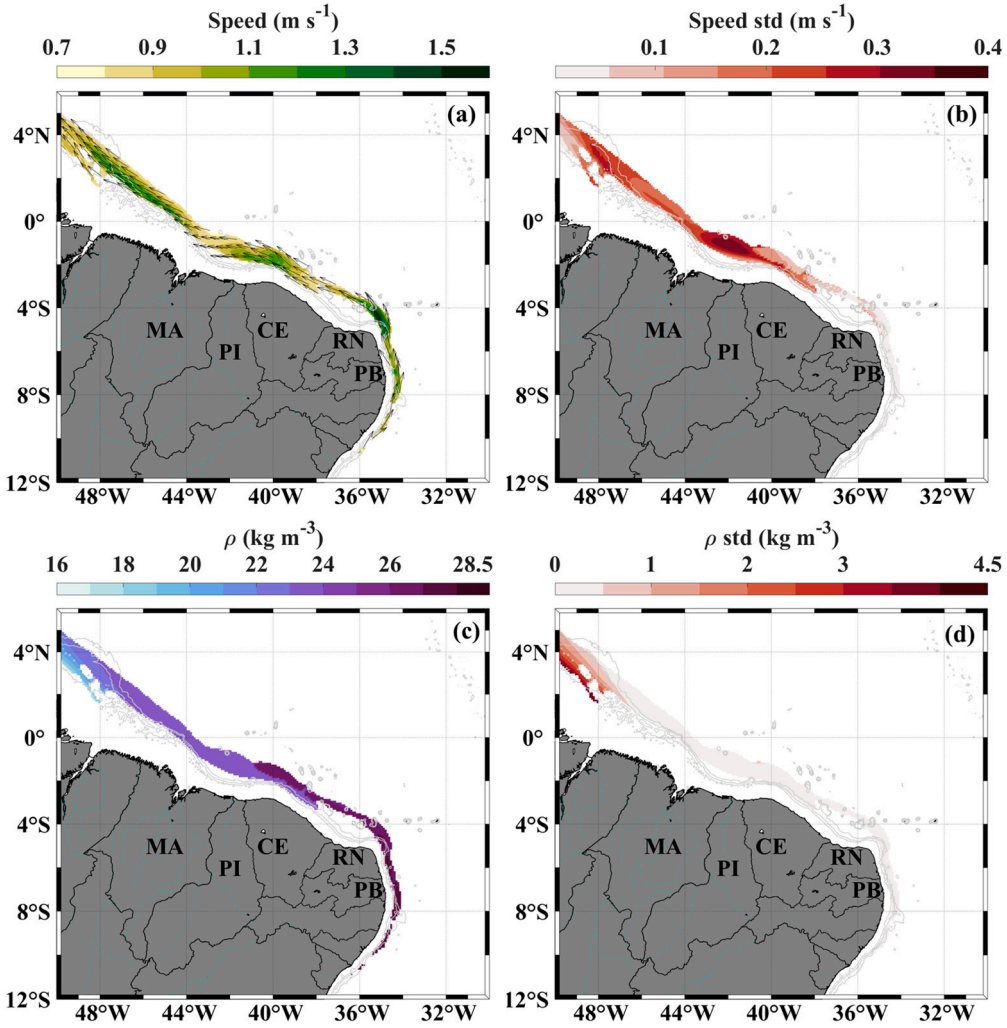

Figure 3. Annual averaged and standard deviation of current velocity ((**a**,**b**), in m·s^{-1}) and seawater density ((**c**,**d**), in kg·m^{-3}) at the depth of Maximum Current Power Density (MCPD) from the climatology. The arrows in (**a**) represent the current direction at the MCPD depth. These maps highlight the spatial variability in flow intensity and water mass structure along the continental margin, revealing dynamic and thermohaline features that influence energy potential across the region.

Figure 4 shows the daily CPD time series for the 12 hotspots over 1993–2025, revealing two distinct temporal regimes. The subsurface hotspots (H1–H3) display comparatively stable CPD with weak seasonality and limited day-to-day excursions, forming persistent energetic signals throughout the record. In contrast, the remaining hotspots (H4–H12) exhibit pronounced short-term variability and strong periodic fluctuations, characterized by

recurrent peaks superimposed on lower background levels and frequent extreme events. These surface-intensified hotspots show greater intermittency, with bursts of high CPD occurring repeatedly across the entire period, indicating that a substantial fraction of their energetic signal is concentrated in episodic events rather than sustained levels. Across all hotspots, the multi-decadal record also indicates intraseasonal variability, with multi-month periods of enhanced or reduced peak activity relative to the long-term behavior, but this modulation is markedly stronger in the seasonally forced hotspots (H4–H12) than in the subsurface group (H1–H3).

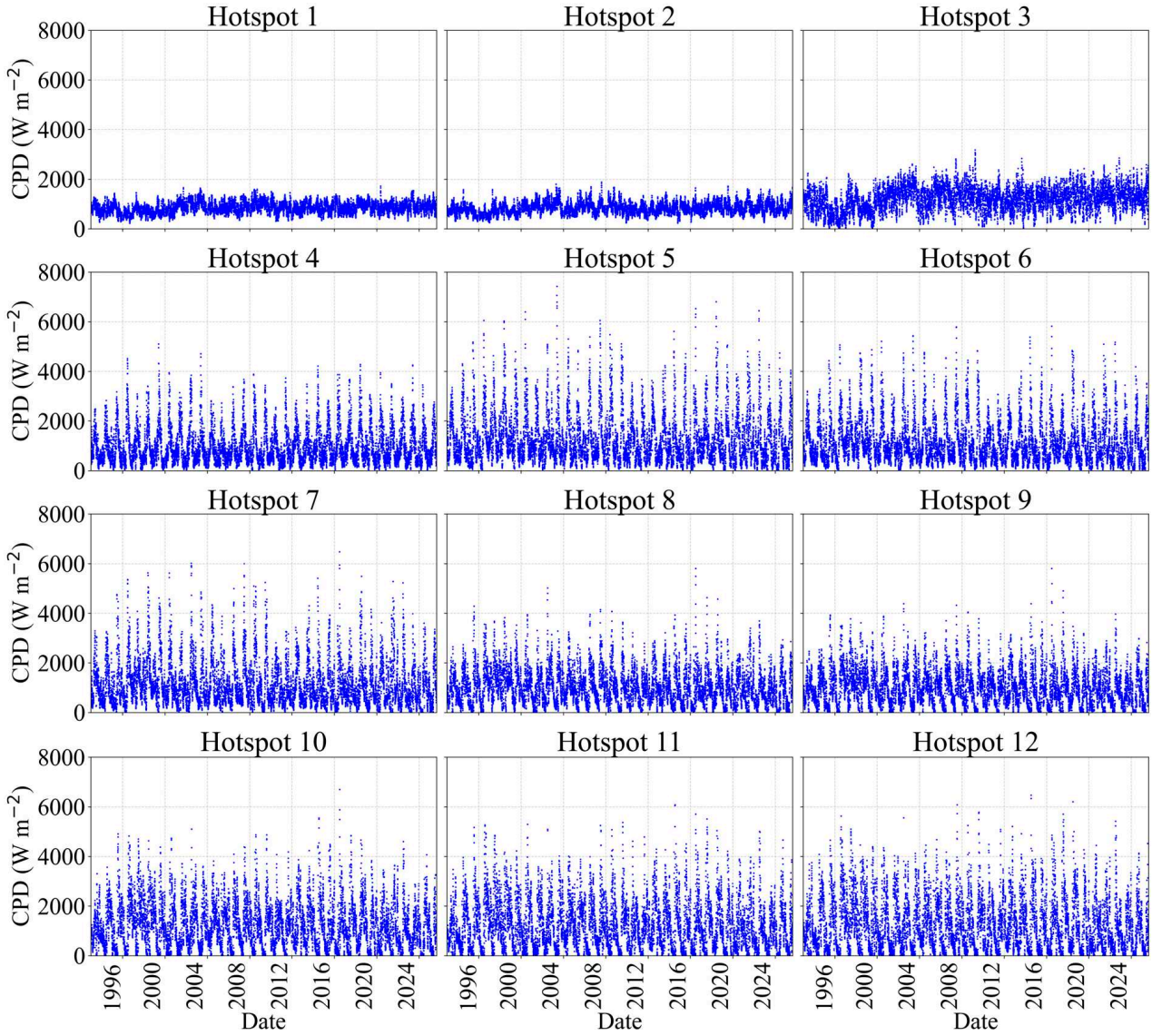

Figure 4. Time series of daily current power density (CPD, in W.m^{-2}) for Hotspots 1 to 12 from 1 January 1993 to 26 August 2025.

Statistical analysis confirmed significant differences among hotspots (ANOVA: $p < 0.0001$). The post hoc test revealed similarity between H1 and H2 ($p = 0.7437$); H3, H10, H11 and H12 ($0.09 < p < 1$); H12 and H5 ($p = 0.3181$); H6 and H7 ($p = 0.9934$); and between H8 and H9 ($p = 0.5803$), while H4 was considered different from all the other hotspots. These differences are illustrated by the CPD boxplots in Figure 5a (see Table 2 for summary statistics) that highlight H1–H2 with median CPD values generally below 1000 W·m^{-2} (~831/808 W·m^{-2}, respectively), and relatively narrow interquartile ranges and fewer extreme events, indicating more stable but lower-magnitude conditions (~1.15/1.05 m·s^{-1}, respectively). H4

had also lower median (730 W·m^{-2}) but with broader dispersion. In contrast, hotspots H5–H12 presented higher medians (H5: ~970 W·m^{-2}; H6/H7: ~886/885 W·m^{-2}; H8–H9: ~924/931 W·m^{-2}; H10/H11/H12: ~1085/1024/1014 W·m^{-2}) coherent with higher speeds (median $\geq$ 1.18 m·s^{-1}), broader dispersion, and numerous high-energy outliers, reflecting both greater energy potential and stronger intermittency (speed range between 0.02–2.43 m·s^{-1}). Furthermore, H3 presented the higher median (~1211 W·m^{-2}) within the hotspots and lower dispersion than the northern group (speed between 0.20–1.83 m·s^{-1}; median ~1.32 m·s^{-1}).

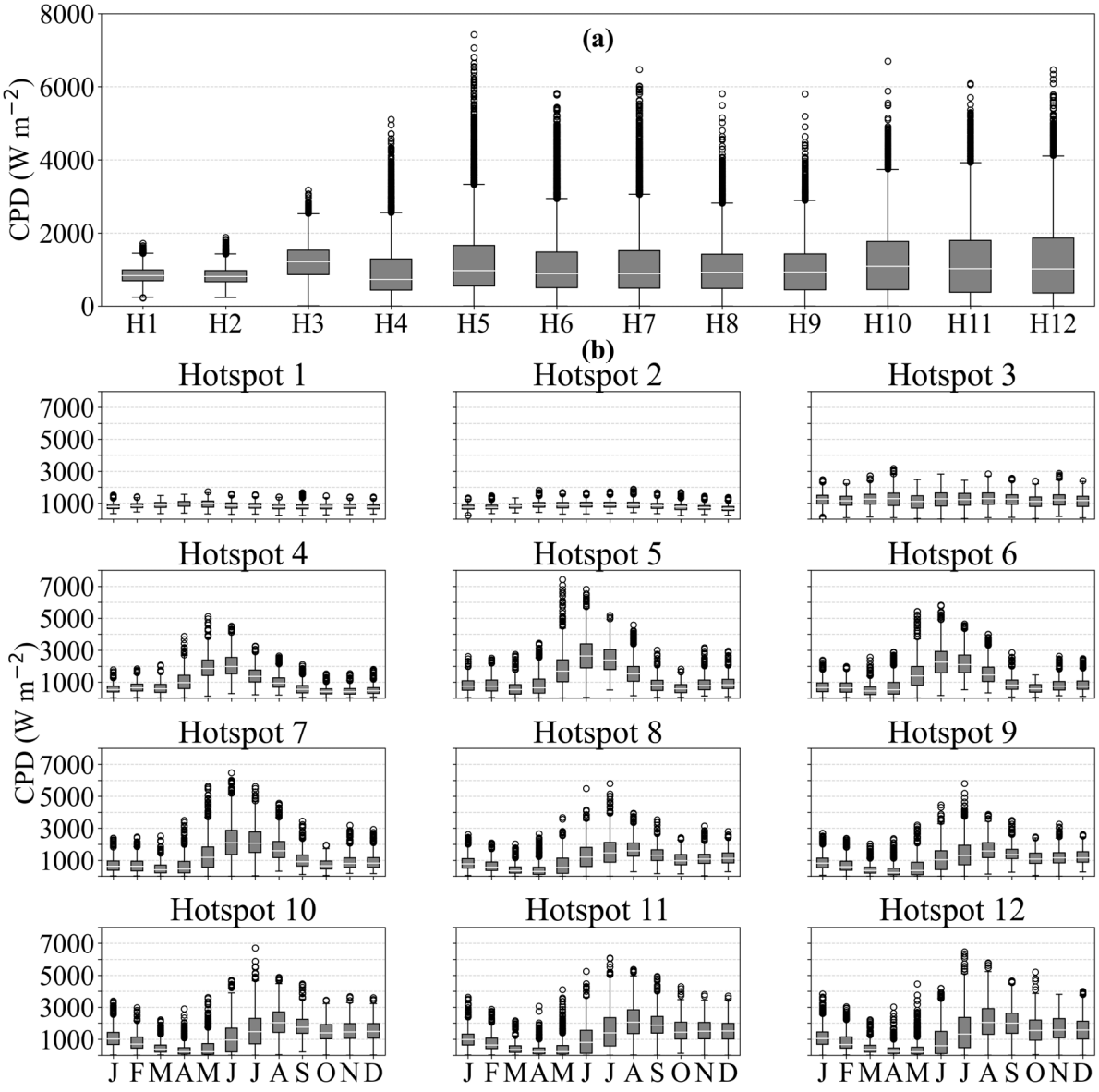

Figure 5. Boxplots of current power density (CPD, in W·m^{-2}) (**a**) over the entire analyzed and (**b**) monthly boxplots for the 12 identified hotspots (H1 to H12). Each box represents the interquartile range (25th to 75th percentile), with the orange line indicating the median. The whiskers extend to the minimum and maximum values that are not considered outliers. Circles represent outliers (values beyond 1.5 times the interquartile range). This figure highlights the variability and magnitude of daily CPD across the hotspots throughout the study period.

The monthly boxplots (Figure 5b) revealed a marked seasonal cycle in the intermediate and high-energy hotspots (except for H1–H3) characterized by elevated CPD from April to July—especially in May and June—followed by a reduction in both magnitude and variabil-

ity starting in September. Conversely, the weakest subsurface hotspots displayed limited seasonal modulation, consistent with their lower variability across the full time series.

Table 2. Summary statistics of daily current power density (CPD) for each hotspot. For every hotspot, the table reports the minimum, maximum, mean, standard deviation, followed by the first quartile (Q1), the median, third quartile (Q3), and interquartile range (IQR). It also lists the lower and upper whiskers used in the boxplots and the number of outliers identified beyond these whiskers (all CPD values in $W \cdot m^{-2}$, except N outliers).

Hotspot	Min ($W \cdot m^{-2}$)	Max ($W \cdot m^{-2}$)	Mean ($W \cdot m^{-2}$)	Std ($W \cdot m^{-2}$)	Q1 ($W \cdot m^{-2}$)	Median ($W \cdot m^{-2}$)	Q3 ($W \cdot m^{-2}$)	IQR ($W \cdot m^{-2}$)	Whisker Low ($W \cdot m^{-2}$)	Whisker High ($W \cdot m^{-2}$)	N Outliers
1	222	1720	845	223	688	831	991	303	244	1443	72
2	233	1877	826	231	662	808	968	306	233	1425	151
3	9	3175	1197	477	862	1211	1527	665	9	2524	37
4	3	5103	956	725	440	730	1287	848	3	2559	496
5	0	7425	1249	985	548	970	1661	1113	0	3330	569
6	1	5823	1114	859	505	886	1479	974	1	2938	534
7	0	6473	1125	894	486	885	1514	1028	0	3055	515
8	1	5807	1020	701	481	924	1415	934	1	2817	224
9	0	5802	998	700	442	931	1422	980	0	2891	170
10	0	6701	1202	906	451	1085	1770	1319	0	3733	127
11	0	6086	1193	964	378	1024	1799	1420	0	3922	136
12	0	6465	1224	1023	356	1014	1859	1503	0	4106	119

The frequency distribution of the CPD time series for each hotspot was evaluated using Weibull PDFs, as shown in Figure 6. The model reproduced the empirical CPD probability density distributions at all hotspots (Figure 6a). Fit performance is consistently high, with Kolmogorov–Smirnov distances ranging from KS D = 0.024–0.072 and CDF-based errors of RMSE = 0.015–0.043 across hotspots. The smallest discrepancies occur in hotspots with compact unimodal distributions (e.g., H7: KS D = 0.024; RMSE = 0.015), whereas the largest deviations occur in hotspots with the strongest long-tail behavior (e.g., H10: KS D = 0.072; RMSE = 0.043). These values indicate that the Weibull function provides an adequate parametric summary of hotspot CPD variability for inter-site comparison.

Weibull parameters varied substantially among hotspots (Figure 6b), indicating distinct distributional regimes the clustered in two regimes: (i) narrower, peaked curves for H1–H3, with more predictable CPD distributions; and (ii) flatter and broader curves for H4–H12, reflecting greater variability and the occurrence of high CPD outliers. Hotspots H1 and H2 exhibited the highest shape parameters ($k > 3.7$), indicating more symmetric and peaked distributions, typical of more stable regimes with lower intermittency. Conversely, the lowest shape values ($k \approx 1.0$–1.4) were observed in hotspots H4, H5–H7, and H10–H12, revealing heavy-tailed, right-skewed distributions, commonly associated with more intermittent CPD patterns and a greater prevalence of extreme events. The scale parameter (λ), which reflects the characteristic CPD intensity, was highest in hotspots H3 and H5 ($\lambda \approx 1342$–1360 $W \cdot m^{-2}$), confirming their higher energy availability. In contrast, H1 and H2 showed lower λ values (<930 $W \cdot m^{-2}$), consistent with their lower medians observed in the boxplots (Figure 5b), but with higher PDFs which implicates in higher power reliability.

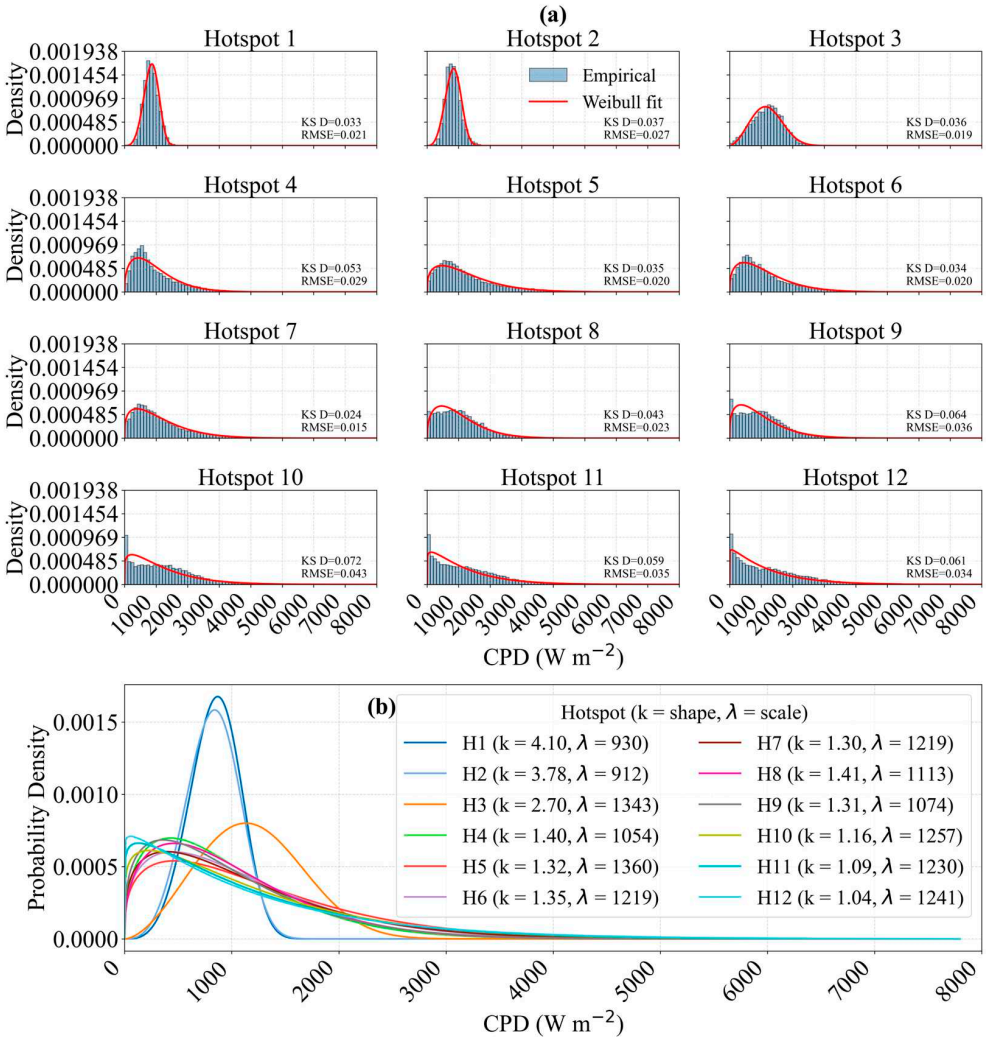

Figure 6. Weibull Probability Density Functions (**a**) fitted to the daily Current Power Density distribution for the 12 identified hotspots. The graphical comparison in (**b**) highlights two distinct energetic regimes: narrower, peaked curves (e.g., H1–H3) indicate higher stability and predictability, while broader, right-skewed curves (e.g., H5–H12) reflect greater variability and the prevalence of extreme energetic events. The shape and scale parameters for the Weibull analysis are provided in (**b**) for reference.

4. Discussion

In this work, 12 hotspots of marine hydrokinetic energy were identified from ocean currents. The Eastern hotspots (H1–H3) are embedded within a region directly dominated by the NBUC and characterized by high-salinity Subtropical Underwater, while the Northern hotspots (H4–H12) are influenced by the NBC and waters from the central South Equatorial Current; these correspond to the same two oceanographic areas identified by Assunção et al. [55] from in situ data. Regarding the Northern Group, the results align closely with the assessment by Shadman et al. [9], who identified the NBC's equatorial margin (Region D) as the most energetic area, reporting annual mean surface velocities of 1.52 m·s^{-1} and seasonal power density peaks exceeding 1400 W·m^{-2} during austral autumn (March–June). The current variability observed also aligns with the NBC seasonal variation reported by Johns et al. [34] from in situ measurements.

In turn, the eastern hotspots identified in this work are reported for the first time, since previous works in this region concerning marine current resource assessment are limited to surface depths (e.g., [9]). In this case, the hotspots were associated with highly local

features characterized by currents with speeds > 1.0 m·s^{-1}. Speeds greater than this value are rarely observed south of 5° S in the NBUC, but frequently reported north of this latitude (e.g., [23,26]). Nevertheless, outside the hotspots, the current estimates—between 0.5–1.0 m·s^{-1} and >1.0 m·s^{-1}, south and north of 5° S, respectively—agree with the observation in previous works with in situ data [26–30]. This suggests that localized bathymetric or dynamical features may play a key role in sustaining the intensified currents observed at the hotspots.

The spatial distribution of the hotspots results from the confluence of large-scale current dynamics, mesoscale features, and localized flow-topography interactions. In this context, the western boundary currents in the SWTA interact strongly with the margin topography, giving rise to vortices, rings, and meanders that strongly enhance eddy kinetic energy and lateral exchange along the continental margin [26,35], which should increase current energy potential and contribute to seasonal variation. Along the margins of the Eastern and Northern Groups off the Brazilian coast, the NBUC flows over a steep continental slope and topographic highs such as the Touros High (from RN state) and adjacent canyons; in this region, the Potiguar Eddy is explicitly associated with the margin physiography and alternates between vortex-like and meandering states, with current–topography interactions near the shelf break inducing disturbances that can reach the mixed layer [37]. Indeed, the location of the hotspots H2 and H3 suggests that they are related to the NBUC shifting with the change in coastline direction that also gives rise to the quasi-stationary Potiguar Eddy [37,56]. In particular, H3 seems to be sustained by the Potiguar Eddy, an anticyclonic eddy with a persistent subsurface structure (100–400 m) centered at ~4° S [56]. The recirculation traps kinetic energy, explaining why H3 presents the highest median power density among all the hotspots. Further south, H1 can also be a result of the NBUC speeding with the change in direction of the coastline, as indicated by change in current speed attributed to the orography effect previously reported south of 7.5° [26]. In the northern sector, Johns et al. [34] reported the acceleration of the NBC as it is constrained by the continental slope, which might explain the northern hotspots close to the shelf break (H4–H12). Nevertheless, the location of the hotspots is also closely related to the change in coastline direction and shelf narrowing.

When an along-shelf current encounters sharp changes in coastline geometry—such as capes, headlands or rapid variations in shelf width—the flow tends to accelerate downstream because of conservation of potential vorticity and simple "nozzle-like" constriction of the current. Laboratory and numerical experiments of rotating, stratified flow past idealized capes show that as the boundary bends or protrudes offshore the streamlines are compressed against the coast and over shallower topography, so the water-column thickness decreases and relative vorticity must adjust; the most efficient way for the current to conserve potential vorticity is to narrow and speed up, forming an intensified jet around and just downstream of the cape [57,58]. High-resolution process studies further demonstrate that this acceleration is often accompanied by strong shear and flow separation in the lee of the headland, which can generate energetic eddies while maintaining a fast, topographically steered core of the boundary current downstream [59]. Similar behavior is seen in real systems such as the California Current upwelling jet, where currents remain attached and intensified along the coast upstream of major capes and then separate and extend offshore as a narrow, high-speed jet downstream, strongly modulating cross-shelf transport [60]. Altogether, these studies indicate that changes in coastline orientation and shelf geometry act to focus momentum, steepen along-shelf pressure gradients and enhance shear, leading to locally accelerated downstream currents relative to adjacent straight-coast segment, therefore increasing MKE potential. Indeed, topographic acceleration was observed near the Touros High (H2), where the NBUC's vertical extension is compressed from ~1000 m to less than 500 m due to shoaling topography [26,37].

Farther south, the BC also interacts with the major topographic features such as Royal Charlotte Bank, Abrolhos Bank and the Vitória–Trindade Ridge, where mesoscale meanders and eddies are generated [35,61], nonetheless, no hotspot was observed in this region. In contrast, the highest CPD values in the domain occurs along the NBUC/NBC at lower latitudes (<10° S), even though local current speeds in the BC can be of similar magnitude to the NBUC. This difference is consistent with low-latitude dynamics: as the Coriolis parameter decreases toward the equator, geostrophic balance becomes more sensitive to changes in pressure gradient and topography, and a given horizontal pressure gradient can support stronger boundary-current velocities [62,63]. Over the upper continental slope, abrupt changes in bathymetry modify the along-slope pressure gradient and potential-vorticity field, producing ageostrophic accelerations and locally intensified jets downstream of banks and sills [64,65]. In the NBUC region, these effects appear to focus the flow into a relatively narrow, topographically steered current, enhancing CPD at MCPD depth, whereas farther south the BC tends to redistribute energy into meanders and eddies as in other mid-latitude boundary systems [66,67], reducing the time-mean CPD along the slope.

Nevertheless, local ADCP measurements [26] show current speeds exceeding those in the reanalysis, indicating that coarse-resolution models may underestimate topographic intensification. For example, Dossa et al. [26] report North Brazil Undercurrent core velocities reaching up to ~1.2 $m \cdot s^{-1}$ off Northeast Brazil and note that the GLORYS12V1 reanalysis shifts the North Brazil Undercurrent core offshore by ~15 km and shows limitations in the near-coastal zone. In the results, the median daily current speed at Hotspots 1 and 2, was 1.15 and 1.05 $m \cdot s^{-1}$, respectively, which is ~4–12% lower than the ~1.2 $m \cdot s^{-1}$ core velocities reported by Dossa et al. [26]. Consequently, the energy potential estimated in this work for the Hotspots 1 and 2—both associated with the NBUC core—is likely conservative in the reanalysis. Although, these two NBUC hotspots were chosen as examples because of ADCP observations in this region; the same observation-based comparison is not directly available for all hotspots. However, while this is not a formal bias estimate (given differences in sampling, location, and the use of core maxima versus medians), it is consistent with the reanalysis capturing the large-scale signal while smoothing peak intensities. Because current power density scales with the cube of velocity, a ~4–12% difference in speed would translate into roughly ~14–49% higher power density, reinforcing that the estimates in this work are conservative lower bounds, particularly near strong topographic gradients.

Beyond average speed differences, however, the full distribution of CPD also holds important implications for energy production and operational reliability. In marine current energy systems, energy production is a nonlinear function of velocity, with power density scaling as the cube of speed. Consequently, even modest changes in the CPD distribution—reflected in the shape of the PDF—directly affect energy availability and turbine performance over time. Therefore, the PDF shape can be interpreted in terms of expected energy yield and the reliability of marine energy resources. The fitted Weibull distributions revealed two contrasting behaviors: the subsurface hotspots exhibit high shape parameters (H1–H3: $k > 2.7$), indicating narrow, peaked distributions centered around high CPD values, which suggest more persistent operating conditions and greater reliability for energy production. In contrast, the remaining hotspots (H4–H12) show lower shape factors ($k \approx 1.0$–1.4), reflecting broader, right-skewed distributions where high-energy events are less frequent but more extreme. This distinction is relevant for device selection and design: high-k regimes support steadier operation around typical conditions, whereas low-k regimes imply stronger intermittency and greater sensitivity to episodic events, favoring solutions that tolerate variable output and benefit from hybridization or complementary generation. This aligns with prior studies that emphasize the importance of probabilistic (distribution-based) resource characterization for tidal/current energy applications and

comparisons across sites [52] and reinforces the value of parametric PDFs for cross-site comparison and technology matching in early-stage assessments.

The difference in PDF shape was related to the hotspot's intrinsic variability: while the northern ones presented strong variability, the eastern ones were more consistently stable along time. For the first, the variability was closely linked to the NBC's seasonal modulation driven by the migration of the ITCZ [34,68] as well as some extreme forcing expected to drive shallow dynamics, as evidenced by the outliers. The NBC intensity reaches its minimum in April and peaks significantly from August to October [34,68], which aligns with the seasonal signal observed in the results, where maximum CPD occurs during the second half of the year. Beyond this prominent seasonal cycle, the ~30-year series also reveals significant intraseasonal variability, with distinct periods exhibiting consistently higher or lower energy peaks than the long-term average. In contrast, the eastern hotspots, which occur in depth (>130 m), do not have marked seasonality, which suggests that the depth provides shelter from the surface atmospheric variability, offering a reliable and stable source of MKE throughout the year. However, seasonality in the shallowing and intensification of the current at the end of the fall and beginning of the austral winter was observed, consistent with previous works [24,26,31]. This apparent stability, despite the expected seasonality can be explained by the interaction between the current system and the regional topography, likely driven by topographic steering and the vertical migration of the current's core. Specifically, the conservation of potential vorticity constrains the flow along the steep bathymetry of the continental slope, anchoring the energy hotspots to fixed isobaths and preventing lateral shifts despite seasonal fluctuations. Furthermore, the observed stability at depth may result from a compensatory mechanism: during periods of NBUC intensification, the current's core typically undergoes seasonal shallowing, while during weaker phases, it deepens. This vertical oscillation can filter the regional seasonal signal at specific depths (>130 m), maintaining a consistent energy flux where the seafloor morphology stabilizes the boundary flow. Nevertheless, these mechanisms remain speculative, and further process-driven investigations, such as high-resolution numerical modeling or dedicated in situ transects, are required to confirm the relative contribution of topography and vertical core displacement to the observed stability.

Furthermore, the distinct patterns of the northern and eastern variability reveal the trade-off between high peak CPD and temporal stability. This is consistent with previous resource assessments and variability studies in wave and tidal energy, which emphasize that not only mean power, but also seasonal and inter-annual variability must be considered when selecting optimal sites [67,69–72]. The statistical distinctions, particularly those revealed by the Weibull analysis, are critical for evaluating hotspot suitability and managing operational risks, offering a compelling analogy to wind energy conversion. Just as wind turbines have 'cut-out' speeds to prevent catastrophic failure during storms, marine devices have operational limits; flow instability—whether directional meandering or turbulence—induces cyclic overloading and pitch oscillations in turbine rotors [16]. These dynamic loads are primary drivers of structural fatigue and system failure, often forcing turbines into survival mode and effectively reducing the exploitable capacity factor. Certainly, the central finding of this study is a clear trade-off between the magnitude of the energy potential and its temporal stability, as quantified by the daily CPD time series analysis. While the NBC offers immense theoretical power to the northern hotspots, with CPD peaks exceeding 7400 $W \cdot m^{-2}$, it also leads to periods of complete intermittency during the low-energy season, which represents a critical economic barrier for energy production [15]. For mature ocean current technologies—exemplified by the US Department of Energy's 'Reference Model 4' designed for the stable Gulf Stream—achieving a competitive Levelized Cost of Energy (LCOE) of ~$0.25/kWh relies heavily on maintaining a high Capacity Factor [73]. The intermittency of the Northern Group would likely degrade

this Capacity Factor, significantly increasing the LCOE compared to this global benchmark. Conversely, the subsurface eastern hotspots, particularly H3, provide a more stable and reliable resource ideal for baseload power generation. H3 presents a 'tuned' resource profile: its median power density (~1211 $W \cdot m^{-2}$) is higher than the typical median of the Northern Group, yet it maintains a tighter distribution, without the destructive tail of extreme events. This balance suggests that H3 offers the high-yield potential of the northern hotspots with the operational safety of the eastern ones, minimizing CapEx risks associated with over-dimensioning equipment [73], i.e., potentially reducing the engineering costs required to withstand extreme outlier events observed in the northern sector. Furthermore, this stability is particularly favorable for advanced technologies like the Cross-stream Active Mooring, which require directional consistency to minimize yaw adjustments and structural fatigue [10].

While these characteristics highlight the engineering relevance of site-specific flow patterns, it is also important to clarify that the CPD values presented here represent the theoretical kinetic energy flux available in the water column, not the technically extractable power. Actual power generation depends on device-specific parameters, including the turbine swept area, the power coefficient and drivetrain efficiency, which are subject to the Betz limit and mechanical losses. Therefore, further studies are needed to translate this theoretical potential into realistic energy yields, considering local flow conditions, device performance, and environmental limitations. In this sense, the CPD results presented here serve as the primary screening parameter for identifying viable sites before technology-specific constraints are applied [74].

Nonetheless, our results have direct implications for early-stage security-informed resource planning because they quantify a fundamental trade-off between peak energy potential and temporal reliability, which maps onto economic feasibility, operational risk, and the capacity to provide dependable supply. In sustainable development frameworks, security is often discussed through integrated environmental, economic, and social pillars [6]; within that framing, a key practical advantage of the stable subsurface hotspots is their potential to support more dependable generation profiles (baseload-like behavior), reducing vulnerability to seasonal intermittency that can undermine capacity factors and increase system costs. Conversely, the highly seasonal northern hotspots highlight that high theoretical power alone does not guarantee dependable supply, emphasizing why probabilistic characterization and long-term variability matter for planning. These outcomes reinforce the value of integrating physical resource assessments into broader marine spatial planning and national energy strategies, while simultaneously motivating targeted observational programs and environmental monitoring to support responsible deployment pathways [7]. In other words, this study provides the physical first-order evidence needed to guide follow-on analyses that explicitly address environmental risk, stakeholder acceptance, and economic performance—components that are central to security-oriented energy transitions but outside the scope of the present oceanographic assessment.

Furthermore, placing these results into a broader setting helps highlight their significance and the need for cautious interpretation. In a global context, the mean CPD values of the northern hotspots (~1.2 $kW \cdot m^{-2}$) are comparable to, though slightly lower than, those reported in world-class locations like the Gulf Stream and Agulhas Current (~2–3 $kW \cdot m^{-2}$) [11]. However, it is critical to note that resource assessments based on global ocean models, like the one used here, have been shown to systematically underestimate current speeds and, consequently, may provide highly conservative estimates of the true energy potential, e.g., VanZwieten et al. [16] reported errors of up to 58% in modeled power density near the surface compared to ADCP data in the Agulhas Current. On the other hand, reanalysis/model datasets are commonly used in renewable-resource studies to complement scarce measurements [75], but multiple studies stress that reanalysis performance is case-dependent and should be carefully

evaluated/validated against observations where possible [75–77]. In addition, limitations can be amplified in complex coastal settings where coarse resolution may not represent locally relevant processes [26,75]. Therefore, the values presented in this study should be considered a robust baseline, with the actual in situ potential likely to be significantly higher.

Lastly, this work is based on a daily reanalysis that, while effective at identifying persistent energetic regions, masks the variability from tides that are important for the northern portion of the study region [78–82]. Similarly, wave-current interactions (WCI) represent another key dynamical factor not explicitly resolved in the reanalysis used. Classic assessments have described the wave climate along the Brazilian coast [83,84], highlighting the energetic influence of the ITCZ in the northern sector where in situ data reveal significant wind-sea and swell systems [85]. This indicates that the interaction between the intense trade wind-driven wave climate and western boundary currents can significantly modulate local hydrodynamics. While this effect is likely negligible for the stable subsurface hotspots (H1–H3) identified here due to their depth (>100 m), it remains a relevant factor for surface device design and operation in the Northern Group.

5. Conclusions

This study aimed to assess the spatial variability and temporal persistence of ocean current energy potential in the Southwestern Tropical Atlantic, using daily reanalysis data to identify robust hotspots and characterize their statistical behavior. The results revealed current energy potential, previously unquantified by surface-only analyses, situated within the broader physics of Western Boundary Current dynamics. The analysis of the Southwestern Tropical Atlantic supports the following four key conclusions:

Resource Dichotomy: Twelve persistent energy hotspots were identified, revealing a clear geographical and dynamical dichotomy between a highly energetic but variable Northern Group (H4–H12), driven by the NBC, and a less potent but significantly more stable Eastern Group (H1–H3), driven by the NBUC.

Subsurface Stability: The results confirm the central hypothesis that the NBUC represents a substantial and reliable energy resource. Its subsurface nature provides shelter from surface atmospheric variability, making the Eastern hotspots particularly attractive for baseload power generation compared to the intermittency observed in the Northern sector.

Optimal Location: Hotspot 3 (H3) emerged as the optimal site, balancing high energy potential with the stability characteristics of the Eastern Group. While the specific flow-topography mechanism responsible for H3 requires further investigation, it presents the highest median current potential (~1211 $W \cdot m^{-2}$) of all identified hotspots.

Strategic Trade-off: The practical exploitation of this resource hinges on a trade-off between the higher theoretical power potential of the northern hotspots and the operational reliability of the eastern ones.

The results confirmed the central hypothesis that the North Brazil Undercurrent represents a substantial and reliable energy resource, with its greater stability making it particularly attractive for baseload power generation. From a practical perspective, the results offer a technical basis to prioritize locations for in situ current monitoring, pre-feasibility studies, and technology adaptation. Furthermore, the findings highlight key characteristics of the hotspots and link their potential to the flow topography interactions driver.

Methodological limitations include the use of rectangular bounding boxes for daily analyses, which improves computational efficiency but may lead to conservative estimates of current power density by including lower-energy areas surrounding the energetic core of each hotspot. In addition, the use of daily reanalysis data is well suited to identify persistent energetic regions but does not resolve tidal variability, which is particularly relevant in the northern part of the study area. The absence of long-term, continuous in situ current

measurements at the hotspot locations further necessitates reliance on reanalysis products, which may locally overestimate or underestimate current speeds and, consequently, power density. Moreover, wave–current interactions are not explicitly resolved in the reanalysis; while this limitation is likely of minor importance for deeper, more stable subsurface hotspots, it remains relevant for the assessment and design of surface-based energy devices in the northern sector.

Gaps and Perspectives

One of the main questions left open in this work is the specific flow–topography interaction mechanism responsible for each hotspot and if the mechanisms can generate hotspots along other continental margins. Addressing this requires targeted investigation of the physical drivers of current intensification, especially in poorly resolved shelf-slope and western boundary current systems. Additionally, the identification of the stable subsurface potential of the NBUC has implications beyond the Southwestern Tropical Atlantic. Many global Western Boundary Currents, such as the Kuroshio, the Gulf Stream, and the Agulhas Current, exhibit similar vertical structures with energetic subsurface cores. While most current projects focus on surface extraction, the results presented here suggest that subsurface optimal zones—protected from surface weather variability and presenting lower turbulence—might represent a globally under-exploited class of renewable resource. Future global assessments should investigate if the stability advantages observed in the NBUC are replicated in these other major current systems, potentially shifting the exploration paradigm from surface-only to stable subsurface baseload resources.

There is also a notable gap in studies of marine current energy in oceanic regions, particularly along the Brazilian coast, where few assessments incorporate cost-per-unit-production estimates or robust observational validation. Compounding this is the lack of continuous in situ current monitoring, especially in the low-latitude Southwestern Tropical Atlantic, which limits the ability to validate model-based energy estimates or detect long-term trends. Therefore, the most critical next step is to initiate long-term, in situ observational programs, including the deployment of moored ADCPs within the identified hotspots. This is essential not only to validate reanalysis-based estimates and support engineering design with high-resolution data, but also to capture the full spectrum of interannual to decadal variability relevant to both energy prospecting and climate science. It is also recommended to integrate ocean energy assessments into broader marine spatial planning and national energy strategies, especially as interest grows in diversifying renewable energy portfolios and exploring hybrid offshore systems.

It is important to note that the apparent temporal stability of eastern hotspots does not imply invariance. The Tropical Atlantic is subject to long-term changes. Brandt et al. [86], for instance, reported a >20% intensification of the Equatorial Undercurrent over a recent decade. Meanwhile, projections indicate that western boundary currents are likely to undergo structural changes due to climate forcing [87–89], although the future trajectory of the North Brazil Current/Undercurrent system—whether acceleration or weakening—remains uncertain. These findings reinforce the need to improve the observational coverage of low-latitude current systems in the SWTA and to systematically account for large-scale climate variability in marine energy assessments. Future research should also explore the role of climate modes such as the Atlantic Niño/Niña and teleconnections from ENSO, in modulating current variability at interannual timescales. Such modes may impact not only the mean resource availability but also its temporal reliability and engineering feasibility.

Ultimately, this work advances the field by moving beyond descriptive surveys to contextualize resource potential within the physical dynamics of western boundary currents. It demonstrates that a comprehensive understanding of both surface and subsurface

flows is essential for accurate marine energy prospecting. By providing a foundational characterization of CPD variability and spatial structure, this study lays the groundwork for the sustainable development of a marine renewable energy sector in Brazil—one that is informed by physics, validated by observations, and robust to climate variability.

Author Contributions: Conceptualization, T.S.L. and S.Q.; methodology, T.S.L. and S.Q.; validation, T.S.L., S.Q., E.J.A.C.L. and M.E.A.I.; formal analysis, T.S.L. and S.Q.; investigation, T.S.L., S.Q., E.J.A.C.L. and M.E.A.I.; resources, M.A. and M.d.C.M.; data curation, T.S.L. and S.Q.; writing—original draft preparation, T.S.L., S.Q., E.J.A.C.L. and M.E.A.I.; writing—review and editing, T.S.L., S.Q., E.J.A.C.L., M.E.A.I., M.A. and M.d.C.M.; visualization, T.S.L. and S.Q.; supervision, S.Q., M.A. and M.d.C.M.; project administration, M.A. and M.d.C.M.; funding acquisition, M.A. and M.d.C.M. All authors have read and agreed to the published version of the manuscript.

Funding: This research is a contribution of the Brazilian Research Network on Global Climate Change FINEP/Rede CLIMA Grant 01.13.0353-00.

Data Availability Statement: The third-party datasets used in this study are publicly available from the Copernicus Marine Service product (DOI: https://doi.org/10.48670/moi-00021), cited in the Methods section.

Acknowledgments: This research is a contribution of the Brazilian Research Network on Global Climate Change FINEP/Rede CLIMA Grant 01.13.0353-00. T.S.L acknowledges the financial support from the Human Resources Program of the Brazilian National Agency for Petroleum, Natural Gas and Biofuels—PRH-ANP-UFPE-FAPESP 38.1. M.A. and S.Q. thank the Center for Synthesis on Environmental and Climate Change-SIMACLIM (MCTI/FNDCT/FINEP 01.22.0584.00). The authors thank the Center for Risk Analysis, Reliability Engineering and Environmental Modeling (CEERMA) for the institutional and logistical support that made this study possible. During the preparation of this manuscript, the authors used ChatGPT 5.1 for the purposes of refine the English language. The authors have reviewed and edited the output and take full responsibility for the content of this publication.

Conflicts of Interest: The authors declare no conflicts of interest.

Abbreviations

The following abbreviations are used in this manuscript:

AAIW	Antarctic Intermediate Water
ADCP	Acoustic Doppler Current Profiler
AMOC	Atlantic Meridional Overturning Circulation
ANOVA	Analysis of Variance
BC	Brazil Current
CapEx	Capital Expenditure
CE	Ceará (State of Brazil)
CF	Capacity Factor
CPD	Current Power Density
CSAM	Cross-stream Active Mooring
cSEC	Central South Equatorial Current
H1–H12	Hotspots 1 to 12
HSD	Honestly Significant Difference
IQR	Interquartile Range
ITCZ	Intertropical Convergence Zone
LCOE	Levelized Cost of Energy
MA	Maranhão (State of Brazil)
MCED	Marine Current Energy Device
MCPD	Maximum Current Power Density
MHK	Marine Hydrokinetic

MLE	Maximum Likelihood Estimation
NBC	North Brazil Current
NBUC	North Brazil Undercurrent
OpEx	Operational Expenditure
PA	Pará (State of Brazil)
PB	Paraíba (State of Brazil)
PDF	Probability Density Function
PE	Pernambuco (State of Brazil) or Potiguar Eddy (context-dependent)
RN	Rio Grande do Norte (State of Brazil)
SEC	South Equatorial Current
sSEC	Southern South Equatorial Current
SUW	Subtropical Underwater
SWTA	Southwestern Tropical Atlantic
WBC	Western Boundary Current

References

1. Lewis, A.; Estefen, S.; Huckerby, J.; Musial, W.; Pontes, T.; Torres-Martinez, J. Ocean Energy. In *IPCC Special Report on Renewable Energy Sources and Climate Change Mitigation*; Edenhofer, O., Pichs-Madruga, R., Sokona, Y., Seyboth, K., Kadner, S., Zwickel, T., Eickemeier, P., Hansen, G., Schlömer, S., von Stechow, C., et al., Eds.; Cambridge University Press: Cambridge, UK, 2011; pp. 533–549. [CrossRef]
2. Clarke, L.; Wei, Y.-M.; de la Vega Navarro, A.; Garg, A.; Hahmann, A.N.; Khennas, S.; Azevedo, I.M.L.; Löschel, A.; Singh, A.K.; Steg, L. Energy Systems. In *Climate Change 2022: Mitigation of Climate Change*; Shukla, P.R., Skea, J., Slade, R., Al Khourdajie, A., van Diemen, R., McCollum, D., Pathak, M., Some, S., Vyas, P., Fradera, R., et al., Eds.; Cambridge University Press: Cambridge, UK, 2022; pp. 613–746.
3. IRENA. *Renewable Energy Statistics 2025*; International Renewable Energy Agency: Abu Dhabi, United Arab Emirates, 2025.
4. Wu, J.J.; Vijayamohan, V.; Field, R.W. On the potential of ocean energy technologies to contribute to future sustainability. *Discov. Sustain.* **2025**, *6*, 741. [CrossRef]
5. Laws, N.D.; Epps, B.P. Hydrokinetic energy conversion: Technology, research, and outlook. *Renew. Sustain. Energy Rev.* **2016**, *57*, 1245–1259. [CrossRef]
6. Chomać-Pierzecka, E.; Błaszczak, B.; Godawa, S.; Kęsy, I. Human Safety in Light of the Economic, Social and Environmental Aspects of Sustainable Development—Determination of the Awareness of the Young Generation in Poland. *Sustainability* **2025**, *17*, 6190. [CrossRef]
7. Copping, A.E.; Martínez, M.L.; Hemery, L.G.; Hutchison, I.; Jones, K.; Kaplan, M. Recent Advances in Assessing Environmental Effects of Marine Renewable Energy Around the World. *Mar. Technol. Soc. J.* **2024**, *58*, 70–87. [CrossRef]
8. Martínez, M.L.; Chávez, V.; Silva, R.; Heckel, G.; Garduño-Ruiz, E.P.; Wojtarowski, A.; Vázquez, G.; Pérez-Maqueo, O.; Maximiliano-Cordova, C.; Salgado, K.; et al. Assessing the potential of marine renewable energy in Mexico: Socioeconomic needs, energy potential, environmental concerns, and social perception. *Sustainability* **2024**, *16*, 7059. [CrossRef]
9. Shadman, M.; Silva, C.; Faller, D.; Wu, Z.; de Freitas Assad, L.; Landau, L.; Levi, C.; Estefen, S. Ocean Renewable Energy Potential, Technology, and Deployments: A Case Study of Brazil. *Energies* **2019**, *12*, 3658. [CrossRef]
10. Tsao, C.-C.; Feng, A.-H.; Hsieh, C.; Fan, K.-H. Marine current power with Cross-stream Active Mooring: Part I. *Renew. Energy* **2017**, *109*, 144–154. [CrossRef]
11. Fraenkel, P.L. Power from marine currents. *Proc. Inst. Mech. Eng. Part A J. Power Energy* **2002**, *216*, 1–14. [CrossRef]
12. Khan, M.Z.A.; Khan, H.A.; Aziz, M. Harvesting Energy from Ocean: Technologies and Perspectives. *Energies* **2022**, *15*, 3456. [CrossRef]
13. Lago, L.I.; Ponta, F.L.; Chen, L. Advances and trends in hydrokinetic turbine systems. *Energy Sustain. Dev.* **2010**, *14*, 287–296. [CrossRef]
14. Ueno, T.; Nagaya, S.; Shimizu, M.; Saito, H.; Murata, S.; Handa, N. Development and demonstration test for floating type ocean current turbine system conducted in Kuroshio Current. In Proceedings of the OCEANS 2018 MTS/IEEE Kobe Techno-Oceans (OTO), Kobe, Japan, 28–31 May 2018; pp. 1–6. [CrossRef]
15. Rourke, F.O.; Boyle, F.; Reynolds, A. Marine current energy devices: Current status and possible future applications in Ireland. *Renew. Sustain. Energy Rev.* **2010**, *14*, 1026–1036. [CrossRef]
16. VanZwieten, J.H.; Baxley, W.E.; Alsenas, G.M.; Meyer, I.; Muglia, M.; Lowcher, C.; Bane, J.; Gabr, M.; He, R.; Hudon, T.; et al. SS Marine Renewable Energy—Ocean Current Turbine Mooring Considerations. In Proceedings of the Offshore Technology Conference, Houston, TX, USA, 4–7 May 2015. [CrossRef]
17. Hsu, T.-W.; Liau, J.-M.; Liang, S.-J.; Tzang, S.-Y.; Doong, D.-J. Assessment of Kuroshio current power test site of Green Island, Taiwan. *Renew. Energy* **2015**, *81*, 853–863. [CrossRef]

18. Haas, K.; Fritz, H.M.; French, S.P.; Neary, V.S. *Assessment of Energy Production Potential from Ocean Currents Along the United States Coastline*; Report No. DOE/EE/2661-10; Georgia Institute of Technology: Atlanta, GA, USA, 2013. [CrossRef]
19. Sadoughipour, M.; VanZwieten, J.; Tang, Y. Drifter-based global ocean current energy resource assessment. *Renew. Energy* **2025**, *244*, 122576. [CrossRef]
20. Schott, F.A.; Fischer, J.; Stramma, L. Transports and Pathways of the Upper-Layer Circulation in the Western Tropical Atlantic. *J. Phys. Oceanogr.* **1998**, *28*, 1904–1928. [CrossRef]
21. Bane, J.M.; He, R.; Muglia, M.; Lowcher, C.F.; Gong, Y.; Haines, S.M. Marine Hydrokinetic Energy from Western Boundary Currents. *Annu. Rev. Mar. Sci.* **2017**, *9*, 105–123. [CrossRef]
22. Lowcher, C.F.; Muglia, M.; Bane, J.M.; He, R.; Gong, Y.; Haines, S.M. Marine Hydrokinetic Energy in the Gulf Stream Off North Carolina: An Assessment Using Observations and Ocean Circulation Models. In *Marine Renewable Energy*; Yang, Z., Copping, A., Eds.; Springer: Cham, Switzerland, 2017; pp. 237–258. [CrossRef]
23. Schott, F.A.; Dengler, M.; Zantopp, R.; Stramma, L.; Fischer, J.; Brandt, P. The Shallow and Deep Western Boundary Circulation of the South Atlantic at 5°–11° S. *J. Phys. Oceanogr.* **2005**, *35*, 2031–2053. [CrossRef]
24. Veleda, D.; Araujo, M.; Zantopp, R.; Montagne, R. Intraseasonal variability of the North Brazil Undercurrent forced by remote winds. *J. Geophys. Res. Ocean.* **2012**, *117*, C11024. [CrossRef]
25. Pereira, J.; Gabioux, M.; Almeida, M.M.; Cirano, M.; Paiva, A.M.; Aguiar, A.L. The Bifurcation of The Western Boundary Current System of The South Atlantic Ocean. *Rev. Bras. Geophys.* **2014**, *32*, 241. [CrossRef]
26. Dossa, A.N.; Silva, A.C.; Chaigneau, A.; Eldin, G.; Araujo, M.; Bertrand, A. Near-surface western boundary circulation off Northeast Brazil. *Prog. Oceanogr.* **2021**, *190*, 102475. [CrossRef]
27. da Silveira, I.C.A.; de Miranda, L.B.; Brown, W.S. On the origins of the North Brazil Current. *J. Geophys. Res. Ocean.* **1994**, *99*, 22501–22512. [CrossRef]
28. Stramma, L.; Fischer, J.; Reppin, J. The North Brazil Undercurrent. *Deep Sea Res. Part I Oceanogr. Res. Pap.* **1995**, *42*, 773–795. [CrossRef]
29. Hummels, R.; Brandt, P.; Dengler, M.; Fischer, J.; Araujo, M.; Veleda, D.; Durgadoo, J.V. Interannual to decadal changes in the western boundary circulation in the Atlantic at 11° S. *Geophys. Res. Lett.* **2015**, *42*, 7615–7622. [CrossRef]
30. Cabré, A.; Pelegrí, J.L.; Vallès-Casanova, I. Subtropical-Tropical Transfer in the South Atlantic Ocean. *J. Geophys. Res. Ocean.* **2019**, *124*, 4820–4837. [CrossRef]
31. Rodrigues, R.R.; Rothstein, L.M.; Wimbush, M. Seasonal Variability of the South Equatorial Current Bifurcation in the Atlantic Ocean: A Numerical Study. *J. Phys. Oceanogr.* **2007**, *37*, 16–30. [CrossRef]
32. Bourlès, B.; Molinari, R.L.; Johns, E.; Wilson, W.D.; Leaman, K.D. Upper layer currents in the western tropical North Atlantic (1989–1991). *J. Geophys. Res. Ocean.* **1999**, *104*, 1361–1375. [CrossRef]
33. Neto, A.V.N.; da Silva, A.C. Seawater temperature changes associated with the North Brazil current dynamics. *Ocean Dyn.* **2014**, *64*, 13–27. [CrossRef]
34. Johns, W.E.; Lee, T.N.; Beardsley, R.C.; Candela, J.; Limeburner, R.; Castro, B. Annual Cycle and Variability of the North Brazil Current. *J. Phys. Oceanogr.* **1998**, *28*, 103–128. [CrossRef]
35. Lima, M.O.; Cirano, M.; Mata, M.M.; Goes, M.; Goni, G.; Baringer, M. An assessment of the Brazil Current baroclinic structure and variability near 22° S in Distinct Ocean Forecasting and Analysis Systems. *Ocean Dyn.* **2016**, *66*, 893–916. [CrossRef]
36. Veleda, D.; Araújo, M.; Silva, M.; Montagne, R. Seasonal and interannual variability of the southern south Equatorial Current bifurcation and meridional transport along the eastern brazilian edge. *Trop. Oceanogr.* **2011**, *39*, 27–59. [CrossRef]
37. Damasceno, Ú.M.; Cintra, M.M.; Gomes, M.P.; Vital, H. Interactions between the North Brazilian Undercurrent (NBUC) and the Southwest Atlantic Margin. Implications for Brazilian shelf-edge systems. *Reg. Stud. Mar. Sci.* **2022**, *54*, 102486. [CrossRef]
38. Zembruscki, S.G.; Barreto, H.T.; Palma, J.C.; Milliman, J.D. Estudo preliminar das províncias geomorfológicas da margem continental brasileira. *An. Congr. Bras. Geol.* **1972**, *26*, 187–209. Available online: https://www.sbgeo.org.br/assets/admin/imgCk/files/Anais/ANAIS%20DO%20XXVI%20CBG_1972_V2.pdf (accessed on 27 November 2025).
39. Coutinho, P.N. *Levantamento do Estado da arte da Pesquisa dos Recursos Vivos Marinhos do Brasil-Oceanografia Geológica; Região Nordeste; Programa REVIZEE*; Ministério Do Meio Ambiente: Brasília, Brazil, 1996; 97p.
40. Buarque, B.V.; Barbosa, J.A.; Magalhães, J.R.G.; Cruz Oliveira, J.T.; Filho, O.J.C. Post-rift volcanic structures of the Pernambuco Plateau, northeastern Brazil. *J. South Am. Earth Sci.* **2016**, *70*, 251–267. [CrossRef]
41. Silva, M.V.B.; Ferreira, B.; Maida, M.; Queiroz, S.; Silva, M.; Varona, H.L.; Araújo, T.C.M.; Araújo, M. Flow-topography interactions in the western tropical Atlantic boundary off Northeast Brazil. *J. Mar. Syst.* **2022**, *227*, 103690. [CrossRef]
42. Stramma, L.; Schott, F. The mean flow field of the tropical Atlantic Ocean. *Deep Sea Res. Part II Top. Stud. Oceanogr.* **1999**, *46*, 279–303. [CrossRef]
43. Stramma, L.; England, M. On the water masses and mean circulation of the South Atlantic Ocean. *J. Geophys. Res. Ocean.* **1999**, *104*, 20863–20883. [CrossRef]
44. Talley, L.D. Antarctic intermediate water in the South Atlantic. In *The South Atlantic*; Wefer, G., Berger, W.H., Siedler, G., Webb, D.J., Eds.; Springer: Berlin/Heidelberg, Germany, 1996; pp. 219–238.

45. Lellouche, J.-M.; Eric, G.; Romain, B.-B.; Gilles, G.; Angélique, M.; Marie, D.; Clément, B.; Mathieu, H.; Olivier, L.G.; Charly, R.; et al. The Copernicus Global 1/12° Oceanic and Sea Ice GLORYS12 Reanalysis. *Front. Earth Sci.* **2021**, *9*, 698876. [CrossRef]
46. Chassignet, E.P.; Hurlburt, H.E.; Smedstad, O.M.; Halliwell, G.R.; Hogan, P.J.; Wallcraft, A.J.; Baraille, R.; Bleck, R. The HYCOM (HYbrid Coordinate Ocean Model) data assimilative system. *J. Mar. Syst.* **2007**, *65*, 60–83. [CrossRef]
47. Forget, G.; Campin, J.M.; Heimbach, P.; Hill, C.N.; Ponte, R.M.; Wunsch, C. ECCO version 4: An integrated framework for non-linear inverse modeling and global ocean state estimation. *Geosci. Model Dev.* **2015**, *8*, 3071–3104. [CrossRef]
48. Cowles, G.W.; Hakim, A.R.; Churchill, J.H. A comparison of numerical and analytical predictions of the tidal stream power resource of Massachusetts, USA. *Renew. Energy* **2017**, *114*, 215–228. [CrossRef]
49. Jaccard, P. Étude comparative de la distribution florale dans une portion des Alpes et des Jura. *Bull. Soc. Vaudoise Sci. Nat.* **1901**, *37*, 547–579.
50. Justus, C.G.; Hargraves, W.R.; Mikhail, A.; Graber, D. Methods for Estimating Wind Speed Frequency Distributions. *J. Appl. Meteorol.* **1978**, *17*, 350–353. [CrossRef]
51. Kirinus, E.P.; Marques, W.C. Viability of the application of marine current power generators in the south Brazilian shelf. *Appl. Energy* **2015**, *155*, 23–34. [CrossRef]
52. Ashkenazy, Y.; Gildor, H. On the probability and spatial distribution of ocean surface currents. *J. Phys. Oceanogr.* **2011**, *41*, 2295–2306. [CrossRef]
53. Virtanen, P.; Gommers, R.; Oliphant, T.E.; Haberland, M.; Reddy, T.; Cournapeau, D.; Burovski, E.; Peterson, P.; Weckesser, W.; Bright, J.; et al. SciPy 1.0: Fundamental algorithms for scientific computing in Python. *Nat. Methods* **2020**, *17*, 261–272. [CrossRef]
54. Seguro, J.V.; Lambert, T.W. Modern estimation of the parameters of the Weibull wind speed distribution for wind energy analysis. *J. Wind Eng. Ind. Aerodyn.* **2000**, *85*, 75–84. [CrossRef]
55. Assunção, R.V.; Silva, A.C.; Roy, A.; Bourlès, B.; Silva, C.H.S.; Ternon, J.-F.; Araujo, M.; Bertrand, A. 3D characterisation of the thermohaline structure in the southwestern tropical Atlantic derived from functional data analysis of in situ profiles. *Prog. Oceanogr.* **2020**, *187*, 102399. [CrossRef]
56. Krelling, A.P.M.; da Silveira, I.C.A.; Polito, P.S.; Gangopadhyay, A.; Martins, R.P.; Lima, J.A.M.; Marin, F.O. A Newly Observed Quasi-stationary Subsurface Anticyclone of the North Brazil Undercurrent at 4° S: The Potiguar Eddy. *J. Geophys. Res. Ocean.* **2020**, *125*, e2020JC016268. [CrossRef]
57. Boyer, D.L.; Tao, L. On the motion of linearly stratified rotating fluids past capes. *J. Fluid Mech.* **1987**, *180*, 429–449. [CrossRef]
58. Doglioli, A.M.; Griffa, A.; Magaldi, M.G. Numerical study of a coastal current on a steep slope in presence of a cape: The case of the Promontorio di Portofino. *J. Geophys. Res. Ocean.* **2004**, *109*, C12033. [CrossRef]
59. Magaldi, M.G.; Özgökmen, T.M.; Griffa, A.; Chassignet, E.P.; Iskandarani, M.; Peters, H. Turbulent flow regimes behind a coastal cape in a stratified and rotating environment. *Ocean Model.* **2008**, *25*, 65–82. [CrossRef]
60. Castelao, R.M.; Luo, H. Upwelling jet separation in the California Current System. *Sci. Rep.* **2018**, *8*, 16004. [CrossRef] [PubMed]
61. Schmid, C.; Schafer, H.; Podesta, G.; Zenk, W. The Vitória Eddy and its relation to the Brazil Current. *J. Phys. Oceanogr.* **1995**, *25*, 2532–2546. [CrossRef]
62. Gill, A.E.; Adrian, E. *Atmosphere-Ocean Dynamics*; Academic Press: New York, NY, USA, 1982.
63. Cushman-Roisin, B.; Beckers, J.-M. *Introduction to Geophysical Fluid Dynamics: Physical and Numerical Aspects*; Academic Press: Waltham, MA, USA, 2011.
64. Huthnance, J.M. Circulation, exchange and water masses at the ocean margin: The role of physical processes at the shelf edge. *Prog. Oceanogr.* **1995**, *35*, 353–431. [CrossRef]
65. Brink, K.H. Cross-Shelf Exchange. *Annu. Rev. Mar. Sci.* **2016**, *8*, 59–78. [CrossRef]
66. McWilliams, J.C. The nature and consequences of oceanic eddies. In *Ocean Modeling in an Eddying Regime*; Hecht, M.W., Hasumi, H., Eds.; American Geophysical Union: Washington, DC, USA, 2008; pp. 5–15. [CrossRef]
67. Hughes, M.G.; Heap, A.D. National-scale wave energy resource assessment for Australia. *Renew. Energy* **2010**, *35*, 1783–1791. [CrossRef]
68. de Freitas Assad, L.P.; Toste, R.; Böck, C.S.; Nehme, D.M.; Sancho, L.; Soares, A.E.; Landau, L. Ocean climatology at Brazilian Equatorial Margin: A numerical approach. *J. Comput. Sci.* **2020**, *44*, 101159. [CrossRef]
69. Neill, S.P.; Hashemi, M.R. Wave power variability over the northwest European shelf seas. *Appl. Energy* **2013**, *106*, 31–46. [CrossRef]
70. Lewis, M.; Neill, S.P.; Robins, P.E.; Hashemi, M.R. Resource assessment for future generations of tidal-stream energy arrays. *Energy* **2015**, *83*, 403–415. [CrossRef]
71. Neill, S.P.; Hashemi, M.R.; Lewis, M.J. Tidal energy leasing and tidal phasing. *Renew. Energy* **2016**, *85*, 580–587. [CrossRef]
72. Reikard, G.; Robertson, B.; Bidlot, J.-R. Combining wave energy with wind and solar: Short-term forecasting. *Renew. Energy* **2015**, *81*, 442–456. [CrossRef]
73. Neary, V.S.; Lawson, M.; Previsic, M.; Copping, A.; Hallett, K.C.; Labonte, A.; Rieks, J.; Murray, D. *Methodology for Design and Economic Analysis of Marine Energy Conversion (MEC) Technologies*; SAND2014-9040; Sandia National Laboratories: Albuquerque, NM, USA, 2014.

74. Bedard, R.; Previsic, M.; Polagye, B.; Hagerman, G.; Casavant, A.; Tarbell, D. *North America Tidal In-Stream Energy Conversion Technology Feasibility Study*; EPRI Report TP-008-NA; Electric Power Research Institute (EPRI): Palo Alto, CA, USA, 2006.
75. Qiu, L.; Howland, M.F. Quantitative Evaluation of Reanalysis and Numerical Weather Prediction Models for Wind Resource Assessment in Offshore Environments. *Geophys. Res. Atmos.* **2025**, *130*, e2025JD043490. [CrossRef]
76. Kanwal, A.; Tahir, Z.U.R.; Asim, M.; Hayat, N.; Farooq, M.; Abdullah, M.; Azhar, M. Evaluation of reanalysis and analysis datasets against measured wind data for wind resource assessment. *Energy Environ.* **2023**, *34*, 1258–1284. [CrossRef]
77. Samal, R.K. Assessment of wind energy potential using reanalysis data: A comparison with mast measurements. *J. Clean. Prod.* **2021**, *313*, 127933. [CrossRef]
78. Beardsley, R.C.; Candela, J.; Limeburner, R.; Geyer, W.R.; Lentz, S.J.; Castro, B.M.; Cacchione, D.; Carneiro, N. The M2 tide on the Amazon Shelf. *J. Geophys. Res. Ocean.* **1995**, *100*, 2283–2319. [CrossRef]
79. Rockwell Geyer, W.; Beardsley, R.C.; Lentz, S.J.; Candela, J.; Limeburner, R.; Johns, W.E.; Castro, B.M.; Dias Soares, I. Physical oceanography of the Amazon shelf. *Cont. Shelf Res.* **1996**, *16*, 575–616. [CrossRef]
80. Gabioux, M.; Vinzon, S.B.; Paiva, A.M. Tidal propagation over fluid mud layers on the Amazon shelf. *Cont. Shelf Res.* **2005**, *25*, 113–125. [CrossRef]
81. Le Bars, Y.; Lyard, F.; Jeandel, C.; Dardengo, L. The AMANDES tidal model for the Amazon estuary and shelf. *Ocean Model.* **2010**, *31*, 132–149. [CrossRef]
82. Prestes, Y.O.; Silva, A.C.; Jeandel, C. Amazon water lenses and the influence of the North Brazil Current on the continental shelf. *Cont. Shelf Res.* **2018**, *160*, 36–48. [CrossRef]
83. Pianca, C.; Mazzini, P.L.; Siegle, E. Brazilian offshore wave climate based on NWW3 reanalysis. *Braz. J. Oceanogr.* **2010**, *58*, 67–80. [CrossRef]
84. Espindola, R.L.; Araújo, A.M. Wave energy resource of Brazil: An analysis from 35 years of ERA-Interim reanalysis data. *PLoS ONE* **2017**, *12*, e0183501. [CrossRef]
85. Beserra, E.R.; Mendes, A.L.T.; Estefen, S.F.; Parente, C.E. Wave Climate Analysis for a Wave Energy Conversion Application in Brazil. In Proceedings of the ASME 2007 26th International Conference on Offshore Mechanics and Arctic Engineering, San Diego, CA, USA, 10–15 June 2007; pp. 837–844.
86. Brandt, P.; Hahn, J.; Schmidtko, S.; Tuchen, F.P.; Kopte, R.; Kiko, R.; Bourlès, B.; Czeschel, R.; Dengler, M. Atlantic Equatorial Undercurrent intensification counteracts warming-induced deoxygenation. *Nat. Geosci.* **2021**, *14*, 278–282. [CrossRef]
87. Seager, R.; Simpson, I.R. Western boundary currents and climate change. *J. Geophys. Res. Ocean.* **2016**, *121*, 7212–7214. [CrossRef]
88. Yang, H.; Lohmann, G.; Wei, W.; Dima, M.; Ionita, M.; Liu, J. Intensification and poleward shift of subtropical western boundary currents in a warming climate. *J. Geophys. Res. Ocean.* **2016**, *121*, 4928–4945. [CrossRef]
89. Sen Gupta, A.; Stellema, A.; Pontes, G.M.; Taschetto, A.S.; Vergés, A.; Rossi, V. Future changes to the upper ocean Western Boundary Currents across two generations of climate models. *Sci. Rep.* **2021**, *11*, 9538. [CrossRef]